

Polarized image of a rotating black hole in Scalar-Tensor-Vector-Gravity theory

Xin Qin¹, Songbai Chen^{1,2*}, Zelin Zhang¹, Jiliang Jing^{1,2 †}

¹ *Department of Physics, Key Laboratory of Low Dimensional Quantum Structures and Quantum Control of Ministry of Education, Synergetic Innovation Center for Quantum Effects and Applications,*

Hunan Normal University, Changsha, Hunan 410081, People's Republic of China
² *Center for Gravitation and Cosmology, College of Physical Science and Technology, Yangzhou University, Yangzhou 225009, People's Republic of China*

Abstract

The polarized images of a synchrotron emitting ring are studied in the spacetime of a rotating black hole in the Scalar-Tensor-Vector-Gravity (STVG) theory. The black hole owns an additional dimensionless MOG parameter described its deviation from Kerr black hole. The effects of the MOG parameter on the observed polarization vector and Stokes $Q - U$ loops depend heavily on the spin parameter, the magnetic field configuration, the fluid velocity and the observation inclination angle. For the fixed MOG parameter, the changes of the polarization vector in the image plane are similar to those in the Kerr black hole case. The comparison of the polarization images between Kerr-MOG black hole and M87* implies that there remains some possibility for the STVG-MOG theory.

PACS numbers: 04.70.Dy, 95.30.Sf, 97.60.Lf

arXiv:2207.12034v2 [gr-qc] 4 Sep 2022

* Corresponding author: csb3752@hunnu.edu.cn

† jljing@hunnu.edu.cn

I. INTRODUCTION

The black hole images of M87* [1–6] and Sgr A*[7], photographed by the Event Horizon Telescope (EHT), strongly confirm the existence of black holes in our Universe, which have greatly stimulated the study of black hole physics, both theoretically and experimentally. These images achieving a diffraction limited angular resolution bring us a lot of information from the strong field region near black hole. In the first polarized images of the black hole M87* [8, 9], the twisting polarization pattern with prominent rotationally symmetric mode reveals that there is a strong magnetic field around black hole in terms of electrons synchrotron radiations. Moreover, the analysis show that the polarization patterns depend also on the strongly curved spacetime near the black holes. Thus, study of polarized images of black holes is beneficial to probe the matter distribution and the related physical process around black holes [10–28], even check theories of gravity.

Exact description for polarized images of black holes must resort to numerical simulations, which is generally computationally expensive due to the broad parameter surveys and the complicated couplings among astrophysical and relativistic effects. Recently, a simple model of an equatorial ring of magnetized fluid orbiting has been developed to investigate the polarized images of synchrotron emission around Schwarzschild black hole [10] and Kerr black hole [11]. Although only the emission from a single radius r_s is considered, this model can clearly reveal dependence of the polarization signatures on magnetic field configuration, black hole spin and observer inclination. Moreover, with this model, the image of a finite thin disk can be produced by simply summing contributions from individual radii [26, 27]. Thus, this model has been recently applied to study the polarized image of an equatorial emitting ring in various spacetimes, such as, 4D Gauss-Bonnet black hole [12], regular black holes [13], Schwarzschild-Melvin black hole [16], and so on.

The observations of galaxies [29, 30] reveal a discrepancy between the observed dynamics and the amount of luminous matter. Theoretically, this discrepancy can be explained by introducing exotic dark matter. However, to date, there is no exact evidence to confirm the existence of dark matter. Another possible resolution to the discrepancy is a modification of gravity theory. STVG [31] is a kind of fully covariant modified gravity (MOG) theories. This MOG theory contains three gravitational fields: the Einstein metric related to massless tensor graviton, a massless scalar graviton and a massive vector graviton. The STVG-MOG theory [31] has successfully explained the rotation curves of galaxies [32, 33] and the dynamics of galactic clusters [34–36]. Moreover, the gravitational waves in this STVG-MOG theory has been studied [37, 38]. The Schwarzschild-like and Kerr-like black hole solutions in STVG-MOG theory are obtained in [39]. These black hole solutions

have an additional MOG parameter yielded a variable gravitational constant. It is of interest to study the observational effects of black holes in STVG-MOG theory because they could help understand this modified gravity theory and some fundamental issues in physics. Effects of the MOG parameter on the quasinormal modes [40], black hole shadow [41, 42], black hole thermodynamics [43] and other physical processes [44–50] have been studied in the spacetime of Schwarzschild-MOG and Kerr-MOG black holes. This paper aims to study the polarization information in the image of a synchrotron emitting ring around a Kerr-MOG black hole [39] and to probe the effects of the MOG parameter on the polarization image.

The paper is organized as follows: Section II briefly introduces Kerr-MOG black hole and presents formulas to calculate the observed polarization vector in the image plane of an emitting ring in this spacetime. Section III presents the polarization images of a synchrotron emitting ring and probes the effects of the MOG parameter on the polarization image. Finally, this paper ends with a summary.

II. OBSERVED POLARIZATION FIELD IN A KERR-MOG BLACK HOLE SPACETIME

The STVG theory is a covariant modified theory of gravity and its action is composed of scalar, tensor and vector fields [31]

$$S = S_G + S_\phi + S_S, \quad (1)$$

with

$$\begin{aligned} S_G &= -\frac{1}{16\pi} \int \sqrt{-g} \frac{R}{G} d^4x, \\ S_\phi &= -\frac{1}{4\pi} \int \sqrt{-g} \left[\frac{1}{4} B_{\mu\nu} B^{\mu\nu} + V(\phi_\mu \phi^\mu) \right] d^4x, \\ S_S &= -\int \sqrt{-g} \frac{1}{G} \left[\frac{1}{2} g^{\alpha\beta} \left(\frac{\nabla_\alpha G \nabla_\beta G}{G^2} + \frac{\nabla_\alpha \mu \nabla_\beta \mu}{\mu^2} \right) + \frac{V(G)}{G^2} + \frac{V(\mu)}{\mu^2} \right] d^4x. \end{aligned} \quad (2)$$

S_G corresponds to the Einstein gravity action and R is Ricci scalar. S_ϕ is the action of the massive vector field ϕ_μ and $B_{\mu\nu} = \partial_\mu \phi_\nu - \partial_\nu \phi_\mu$. G is a scalar field $G = G_N(1 + \alpha)$ corresponding to a spin 0 massless graviton, G_N is Newton's gravitational constant and α is a dimensionless parameter. In this modified theory, the mass of the vector field ϕ_μ is also an effective spin 0 scalar field μ . $V(G)$ and $V(\mu)$ are self-interaction potentials of μ and G fields, respectively. The spacetime of a rotating black hole in the STVG-MOG theory [31] can be described by the so-called Kerr-MOG metric with the form in Boyer-Lindquist coordinate [39]

$$ds^2 = -\frac{\Delta \rho^2}{\Xi} dt^2 + \frac{\rho^2}{\Delta} dr^2 + \Sigma d\theta^2 + \frac{\Xi \sin^2 \theta}{\rho^2} (d\phi - \omega dt)^2, \quad (3)$$

where

$$\begin{aligned}\Delta &= r^2 - 2GMr + a^2 + \alpha G_N GM^2, & \rho^2 &= r^2 + a^2 \cos^2 \theta, \\ \omega &= \frac{a(a^2 + r^2 - \Delta)}{\Xi}, & \Xi &= (r^2 + a^2)^2 - \Delta a^2 \sin^2 \theta.\end{aligned}\quad (4)$$

Here M and a are the mass parameter and the spin parameter of Kerr-MOG black hole, respectively. The Kerr-MOG metric can reduce to the Kerr metric in the limit $\alpha = 0$. Thus, the parameter α can be used to measure the deviation of Kerr-MOG black hole in STVG-MOG theory from Kerr black hole in general relativity. The Arnowitt-Deser-Misner (ADM) mass and the angular momentum of the Kerr-MOG black hole are given by [48]

$$\mathcal{M} = (1 + \alpha)M, \quad J = \mathcal{M}a. \quad (5)$$

With the ADM mass \mathcal{M} , the function Δ can be rewritten as

$$\Delta = r^2 - 2G_N \mathcal{M}r + a^2 + \frac{\alpha}{1 + \alpha} G_N^2 \mathcal{M}^2. \quad (6)$$

The outer and inner horizon radiuses are the roots of $\Delta = 0$, i.e.,

$$r_{\pm} = \mathcal{M} \pm \sqrt{\frac{\mathcal{M}^2}{1 + \alpha} - a^2}. \quad (7)$$

Here we set $G_N = 1$ without loss of generality. The extremal limit for Kerr-MOG black hole is $\mathcal{M}^2 = (1 + \alpha)a^2$. Similarly, the Kerr-MOG metric is singular at $\rho^2 = 0$ as in the Kerr case.

Now, the polarization vectors are to be studied for photons emitted from the ring with radius r_s around a Kerr-MOG black hole. A synchrotron emitting ring is assumed to lie in the equatorial plane ($\theta_s = \frac{\pi}{2}$). In the local ZAMO frame of the point P in the ring, the four-vector components $V^{(a)}$ of emitter are related to the vector V_{μ} in Kerr-MOG spacetime by [10, 11]

$$V^{(a)} = \eta^{(a)(b)} e_{(b)}^{\mu} V_{\mu}, \quad (8)$$

where $\eta^{(a)(b)}$ is the flat Minkowski metric and $e_{(b)}^{\mu}$ is the zero-angular-momentum-observer (ZAMO) tetrad

$$e_{(b)}^{\mu} = \begin{bmatrix} \frac{1}{r_s} \sqrt{\frac{\Xi_s}{\Delta_s}} & 0 & \frac{\omega_s}{r_s} \sqrt{\frac{\Xi_s}{\Delta_s}} & 0 \\ 0 & \frac{\sqrt{\Delta_s}}{r_s} & 0 & 0 \\ 0 & 0 & \frac{r_s}{\sqrt{\Xi_s}} & 0 \\ 0 & 0 & 0 & -\frac{1}{r_s} \end{bmatrix}. \quad (9)$$

For a boosted emitter in the local orthonormal ZAMO frame, its boosting velocity is assumed to be in the $r - \phi$ plane and has a form

$$\vec{\beta} = \beta_{\nu} [\cos \chi(\hat{r}) + \sin \chi(\hat{\phi})]. \quad (10)$$

The vectors of point emitter in the the boosted orthonormal frame can be obtained by a Lorentz transformation $\Lambda^{(a)}_{(b)}$ from the ZAMO frame, i.e.,

$$V'^{(a)} = \Lambda^{(a)}_{(b)} V^{(b)}, \quad (11)$$

where

$$\Lambda^{(a)}_{(b)} = \begin{bmatrix} \gamma & -\beta_\nu \gamma \cos \chi & -\beta_\nu \gamma \sin \chi & 0 \\ -\beta_\nu \gamma \cos \chi & (\gamma - 1) \cos \chi^2 + 1 & (\gamma - 1) \sin \chi \cos \chi & 0 \\ -\beta_\nu \gamma \sin \chi & (\gamma - 1) \sin \chi \cos \chi & (\gamma - 1) \sin \chi^2 + 1 & 0 \\ 0 & 0 & 0 & 1 \end{bmatrix}, \quad (12)$$

and γ is the Lorentz factor. Thus, the vector of the point source in black hole spacetime can be obtained from the boosted orthonormal frame by an inverse transformation

$$V^\mu = e^\mu_{(c)} \Lambda^{(c)}_{(a)} V'^a. \quad (13)$$

where $\Lambda^{(b)}_{(a)}$ is the inverse matrix of $\Lambda^{(a)}_{(b)}$. Here, the orientation $(\hat{x}, \hat{y}, \hat{z})$ is equivalent to $(\hat{r}, \hat{\phi}, \hat{\theta})$.

To study the polarized image of an equatorial emitting ring around a Kerr-MOG black hole, the null geodesic describing photon propagation must be solved firstly. Using the Hamilton-Jacobi approach, the null geodesic equation in Kerr-MOG black hole spacetime can be expressed as

$$\begin{aligned} \frac{\rho^2}{E} p^t &= \frac{r^2 + a^2}{\Delta} (r^2 + a^2 - a\lambda) + a(\lambda - a \sin^2 \theta), \\ \frac{\rho^2}{E} p^\phi &= \frac{a}{\Delta} (r^2 + a^2 - a\lambda) + \frac{\lambda}{\sin^2 \theta} - a, \\ \frac{\rho^2}{E} p^r &= \pm_r \sqrt{\mathcal{R}(r)}, \\ \frac{\rho^2}{E} p^\theta &= \pm_\theta \sqrt{\Theta(\theta)}. \end{aligned} \quad (14)$$

The conserved quantities λ and η correspond to the energy-rescaled angular momentum parallel to the axis of symmetry and Carter constant, respectively. The radial potential $\mathcal{R}(r)$ and the angular potential $\Theta(\theta)$ can be expressed as

$$\begin{aligned} \mathcal{R}(r) &= (r^2 + a^2 - a\lambda)^2 - \Delta [\eta + (a - \lambda)^2], \\ \Theta(\theta) &= \eta + a^2 \cos^2 \theta - \lambda^2 \cot^2 \theta. \end{aligned} \quad (15)$$

The photon trajectory is determined by its initial position, the conserved quantities λ, η , and the signs \pm_r, \pm_θ of its initial motion. The photon's four-momentum can be given by

$$p_\mu dx^\mu = -dt \pm_r \frac{\sqrt{\mathcal{R}(r)}}{\Delta(r)} dr \pm_\theta \sqrt{\Theta(\theta)} d\theta + \lambda d\phi. \quad (16)$$

In the Kerr-MOG black hole spacetime (3), the celestial coordinates (x, y) for the photon's arrival position on the observer's screen are

$$x = -\frac{\lambda}{\sin \theta_o}, \quad y = \pm_o \sqrt{\Theta(\theta)}, \quad (17)$$

where angel θ_o is the observer's polar inclination from the normal direction of the accretion disk and \pm_o is the sign of p^θ .

As the photon emitted from the initial position (r_s, θ_s) moves along the null geodesic to the observer at position (r_o, θ_o) , its trajectory is given by the null geodesic equation (14) [11, 51]

$$I_r \equiv \int_{r_s}^{r_o} \frac{dr}{\pm_r \sqrt{\mathcal{R}(r)}} = \int_{\theta_s}^{\theta_o} \frac{d\theta}{\pm_\theta \sqrt{\Theta(\theta)}} \equiv G_\theta. \quad (18)$$

Here, the slash denotes that the sign of $\pm_r = \text{sign}(p^r)$ or $\pm_\theta = \text{sign}(p^\theta)$ in the path integral change at radial or angular turning point. For a photon's trajectory with m turning points in θ and $\theta_s = \frac{\pi}{2}$, the null geodesic equation can be simplified as [11, 51]

$$\sqrt{-u_- a^2} I_r + \text{sign}(\beta) F_o = 2mK \left(\frac{u_+}{u_-} \right), \quad (19)$$

with

$$F_o = F \left(\arcsin \frac{\cos \theta_o}{\sqrt{u_+}} \middle| \frac{u_+}{u_-} \right), \quad u_\pm = \Delta_\theta \pm \sqrt{\Delta_\theta^2 + \frac{\eta}{a^2}}, \quad \Delta_\theta = \frac{1}{2} \left(1 - \frac{\eta + \lambda^2}{a^2} \right), \quad (20)$$

where F and K denote the first-kind incomplete and complete elliptic integrals, respectively. Actually, from the geodesic equation (19), an inversion formula for the emission radius $r_s(I_r)$ can be obtained [51]

$$r_s(I_r) = \frac{r_4 r_{31} - r_3 r_{41} \text{sn}^2(\frac{1}{2} \sqrt{r_{31} r_{42}} I_r - \mathcal{F}_o | k)}{r_{31} - r_{41} \text{sn}^2(\frac{1}{2} \sqrt{r_{31} r_{42}} I_r - \mathcal{F}_o | k)}, \quad (21)$$

where

$$\mathcal{F}_o = F \left(\arcsin \sqrt{\frac{r_{31}}{r_{41}}} \middle| k \right), \quad k = \frac{r_{32} r_{41}}{r_{31} r_{42}}, \quad r_{ij} = r_j - r_i. \quad (22)$$

Here r_1, r_2, r_3, r_4 are the four roots of radial potential $\mathcal{R}(r)$ and $\text{sn}(q|k)$ is Jacobi elliptic function. In the Kerr-MOG black hole spacetime (3), the four roots r_1, r_2, r_3, r_4 can also expressed as

$$r_{1,2} = -z \mp \sqrt{-\frac{\mathcal{A}}{2} - z^2 + \frac{\mathcal{B}}{4z}}, \quad r_{3,4} = z \mp \sqrt{-\frac{\mathcal{A}}{2} - z^2 + \frac{\mathcal{B}}{4z}}, \quad (23)$$

where

$$z = \sqrt{\frac{\omega_+ + \omega_-}{2} - \frac{\mathcal{A}}{6}} > 0, \quad \omega_\pm = \sqrt[3]{-\frac{\mathcal{Q}}{2} \pm \sqrt{\left(\frac{\mathcal{P}}{3}\right)^3 + \left(\frac{\mathcal{Q}}{2}\right)}}, \quad (24)$$

$$\mathcal{P} = -\frac{\mathcal{A}^2}{12} - \mathcal{C}, \quad \mathcal{Q} = -\frac{\mathcal{A}}{3} \left[\left(\frac{\mathcal{A}}{6}\right)^2 - \mathcal{C} \right] - \frac{\mathcal{B}^2}{8},$$

with

$$\begin{aligned}\mathcal{A} &= a^2 - \eta - \lambda^2, \\ \mathcal{B} &= \frac{2\mathcal{M}}{1+\alpha} \{\eta + (\lambda - a)^2 + \alpha[\eta + (\lambda - a)^2]\}, \\ \mathcal{C} &= -a^2\eta - \frac{\alpha\mathcal{M}^2}{1+\alpha} [\eta + (\lambda - a)^2].\end{aligned}\tag{25}$$

Combining (19) and (21), one can numerically compute the set of celestial coordinates (x, y) for a photon emitted on an equatorial ring with a radius r_s . The photon four-momentum at the source $(r_s, \theta_s = \frac{\pi}{2})$ can be expressed as

$$p_t = -1, \quad p_r = \pm_r \frac{\sqrt{\mathcal{R}(r_s)}}{\Delta_s}, \quad p_\theta = \pm_s \sqrt{\eta}, \quad p_\phi = \lambda,\tag{26}$$

where the sign of p^θ at the source $\pm_s = (-1)^m \pm_o$. The sign of \pm_r can be computed by a semi-analytic calculation [51]. With the determined sign of p^r , the four-momentum p^μ of photon at the source can be calculated by

$$\begin{aligned}p^t &= \frac{1}{r_s^2} \left[\frac{r_s^2 + a^2}{\Delta_s} (r_s^2 + a^2 - a\lambda) + a(\lambda - a) \right], & p^r &= \pm_r \frac{1}{r_s^2} \sqrt{\mathcal{R}(r_s)}, \\ p^\phi &= \frac{1}{r_s^2} \left[\frac{a}{\Delta_s} (r_s^2 + a^2 - a\lambda) + \lambda - a \right], & p^\theta &= \pm_s \frac{\sqrt{\eta}}{r_s^2}.\end{aligned}\tag{27}$$

Converting the four-momentum p^μ to the local frame of the emitter by (11), the local photon polarization at the source can be obtained. In the local frame, one has $f^t = 0$. For the synchrotron radiation, the spatial components of the photon polarization vector at the source $\vec{f} = (f^r, f^\theta, f^\phi)$ are related to the local three-momentum $\vec{p} = (p^r, p^\theta, p^\phi)$ and the local magnetic field $\vec{B} = (B^r, B^\theta, B^\phi)$ by

$$\vec{f} = \frac{\vec{p} \times \vec{B}}{|\vec{p}|}.\tag{28}$$

The photon polarization vector at the source f^μ in Boyer-Linquist coordinates can be computed through the transformation (13). With the angle ζ between \vec{p} the magnetic field \vec{B}

$$\sin \zeta = \frac{|\vec{p} \times \vec{B}|}{|\vec{p}| |\vec{B}|},\tag{29}$$

the normalized polarization vector satisfies

$$f^\mu f_\mu = \sin^2 \zeta |\vec{B}|^2.\tag{30}$$

In the propagation of photon in the Kerr-MOG black hole spacetime (3), the polarization vector f^μ obeys

$$f^\mu p_\mu = 0, \quad p^\mu \nabla_\mu f^\nu = 0.\tag{31}$$

According to Walker-Penrose theorem [52, 53], along null geodesic in the Kerr-MOG geometry (3), there is a conserved complex quantity

$$\kappa = p^i f^j (l_i n_j - l_j n_i - m_i \bar{m}_j + \bar{m}_i m_j) \Psi_2^{-\frac{1}{3}}, \quad (32)$$

with

$$\kappa = \kappa_1 + i\kappa_2 = (A - iB) \Psi_2^{-\frac{1}{3}}, \quad (33)$$

$$A = (p^t f^r - p^r f^t) + a \sin^2 \theta (p^r f^\phi - p^\phi f^r),$$

$$B = [(r^2 + a^2)(p^\phi f^\theta - p^\theta f^\phi) - a(p^t f^\theta - p^\theta f^t)] \sin \theta.$$

Ψ_2 is Weyl scalar and has a form

$$\Psi_2 = -\frac{\mathcal{M}}{(r - ia \cos \theta)^3} \left[1 - \frac{\alpha \mathcal{M}}{(1 + \alpha)(r + ia \cos \theta)} \right]. \quad (34)$$

Making use of the celestial coordinates (x, y) and the Walker-Penrose constant κ at the source $(r_s, \theta_s = \frac{\pi}{2})$, the polarization vector on the observer's screen can be obtained by [53, 54]

$$f^x = \frac{y\kappa_2 - \mu\kappa_1}{\mu^2 + y^2}, \quad f^y = \frac{y\kappa_1 + \mu\kappa_2}{\mu^2 + y^2}, \quad \mu = -(x + a \sin \theta_o). \quad (35)$$

In general, the intensity of linear polarization for synchrotron radiation that reaches the observer from the source position can be approximated as [10, 11]

$$|I| = g^{3+\alpha_\nu} l_p |\vec{B}|^{1+\alpha_\nu} \sin \zeta^{1+\alpha_\nu}, \quad (36)$$

where g is the redshift factor measured by the ratio of the photon energies at the observer $E_o = 1$ and at the emitter $E_s = p^{(t)}$. The power α_ν depends on the properties of the accretion disk. Here, we set $\alpha_\nu = 1$ as in refs.[10, 11]. The quantity $l_p = \frac{r_s^{(t)}}{p_s^{(z)}} H$ is the geodesic path length through the emitting material. H is the height of the disk which can be taken to be a constant for simplicity. Thus, the observed components of photon polarization vector are

$$f_{obs}^x = \sqrt{l_p} g^2 |B| \sin \zeta f^x, \quad f_{obs}^y = \sqrt{l_p} g^2 |B| \sin \zeta f^y. \quad (37)$$

Finally, the total polarization intensity and the electric vector position angle (EVPA) can be given by

$$I = (f_{obs}^x)^2 + (f_{obs}^y)^2, \quad \text{EVPA} = \frac{1}{2} \arctan \frac{U}{Q}, \quad (38)$$

where Q and U are the Stokes parameters

$$Q = (f_{obs}^y)^2 - (f_{obs}^x)^2, \quad U = -2f_{obs}^x f_{obs}^y. \quad (39)$$

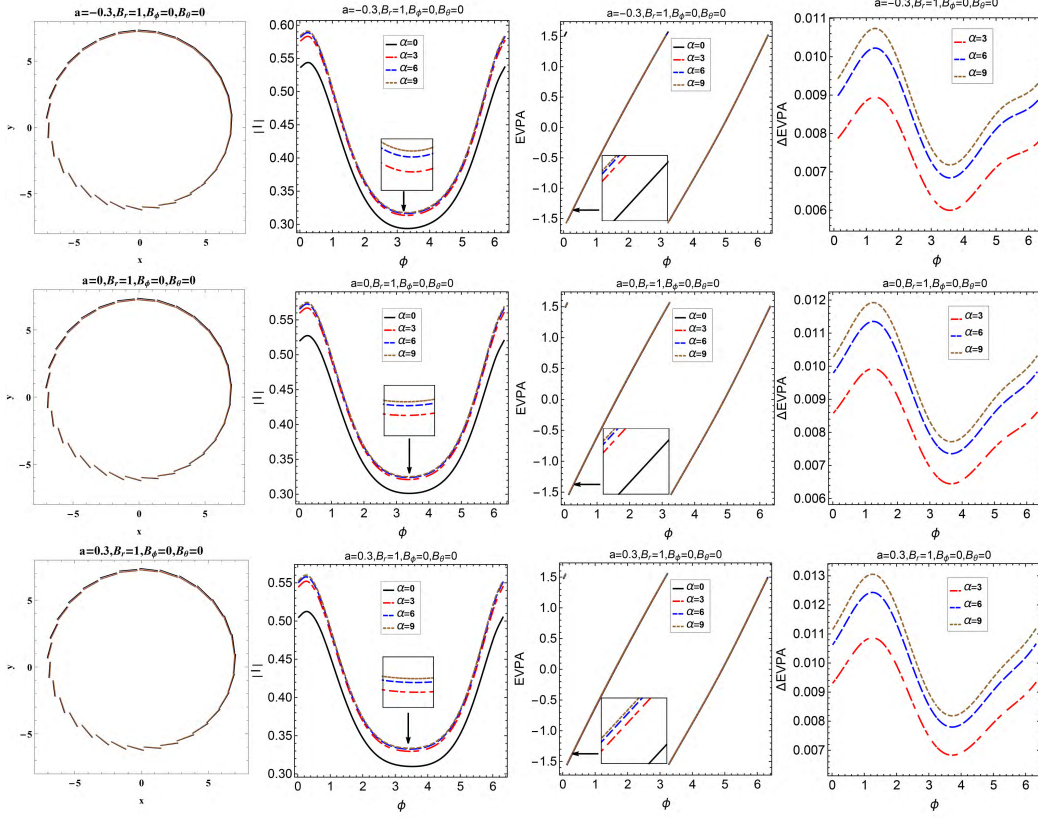


FIG. 1: Effects of the MOG parameter α on the polarized vector and EVPA in the Kerr-MOG black hole spacetime (3) for the magnetic field owned only the radial component B_r . Here we set $\mathcal{M} = 1$, $r_s = 6$, $\theta_o = 20^\circ$, $\beta_\nu = 0.3$, and $\chi = -90^\circ$.

For the Kerr-MOG black hole spacetime (3), combining photon geodesic with Eqs. (32), (36), (37), (38) and (39), the polarization intensity and EVPA in the pixel related to the point source can be obtained. Repeating similar operations along the emitting ring, the total polarization image of the emitting ring around a Kerr-MOG black hole and the corresponding the effects of MOG parameter can be presented.

III. EFFECTS OF MOG PARAMETER ON THE POLARIZED IMAGE OF AN EQUATORIAL EMITTING RING AROUND A KERR-MOG BLACK HOLE

Figs.(1)-(8) present the polarization vector distribution in the image of the emitting ring with radius $r_s = 6$ around a Kerr-MOG black hole. Results show that the polarization vector distribution in the image depends on not only the magnetic field configuration, the motion of fluid particle and the observer's inclination angle, but also on the spin parameter and the MOG parameter α of black hole. Figs.(1)-(5) present the change of the polarized vector and EVPA with the MOG parameter α in the case the magnetic field lies in the equatorial plane for the fixed parameters $r = 6$, $\theta_o = 20^\circ$, $\beta_\nu = 0.3$ and $\chi = -90^\circ$. For the case with only radial magnetic field, Fig.(1) shows that the polarization intensity and the EVPA increase with the MOG parameter

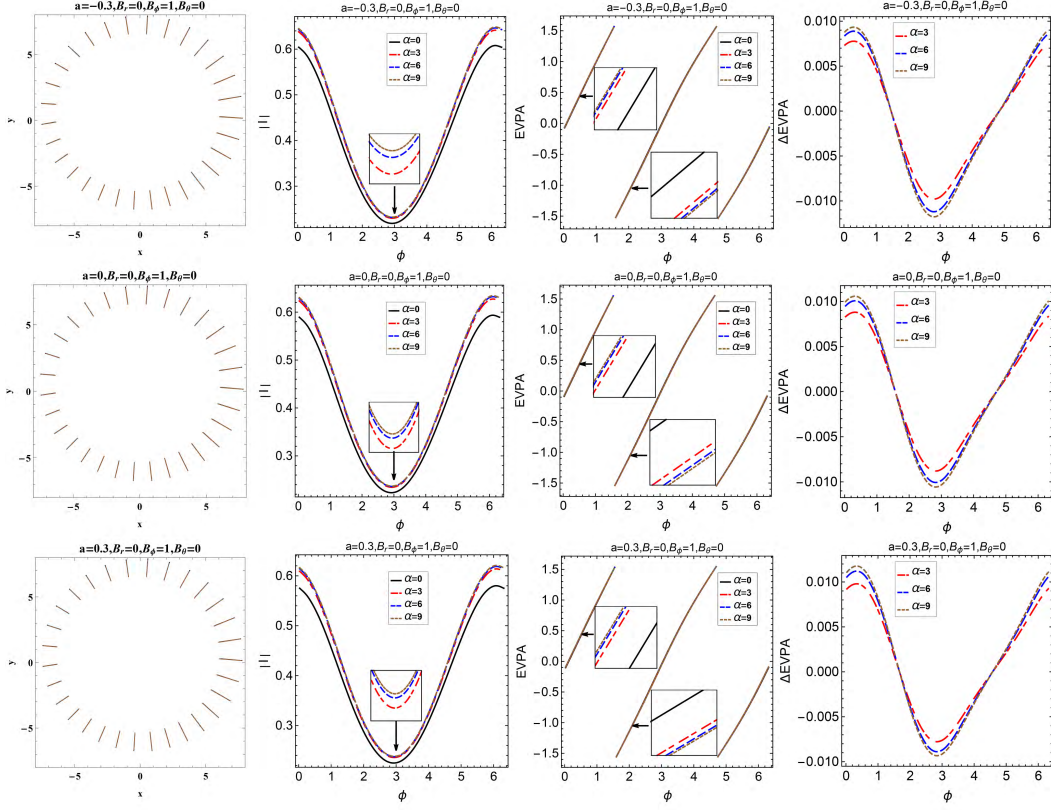


FIG. 2: Effects of the MOG parameter α on the polarized vector and EVPA in the Kerr-MOG black hole spacetime (3) for the equatorial magnetic field owned only the angular component B_ϕ . Here we set $\mathcal{M} = 1$, $r_s = 6$, $\theta_o = 20^\circ$, $\beta_\nu = 0.3$, and $\chi = -90^\circ$.

α . The quantity $\Delta\text{EVPA} \equiv \text{EVPA} - \text{EVPA}_K$, described the EVPA difference between in Kerr-MOG and Kerr spacetimes, increases with the parameter α . In the cases with different spin parameters, the change of the polarization image feature with α is qualitatively similar in the Kerr-MOG spacetime. For the case with only angular magnetic field, Fig.(2) indicates that the polarization intensity increase with the MOG parameter α . However, EVPA increases with α as the azimuthal coordinate ϕ lies in the region $(0, \frac{\pi}{2}) \cup (\frac{3\pi}{2}, 2\pi)$, but decreases with α as the azimuthal coordinate $\phi \in (\frac{\pi}{2}, \frac{3\pi}{2})$. For the equatorial magnetic field with nonzero radial and angular components, from Fig.(3), the polarization intensity still increases with α . The change of EVPA becomes more complicated. With the increasing of the ratio B_r/B_ϕ , the region where EVPA increases with α becomes broad so that EVPA finally becomes a increasing function of α .

Fig.(4) presents the effects of MOG parameter α on the polarized images for different fluid direction angle χ . For the different χ , the polarization intensity still increases with α . However, as the angle χ changes from -120° to $\chi = -180^\circ$, the region where EVPA increases with α becomes narrow and then EVPA finally becomes a decreasing function of α . The effects of MOG parameter α on the polarized vector and EVPA for

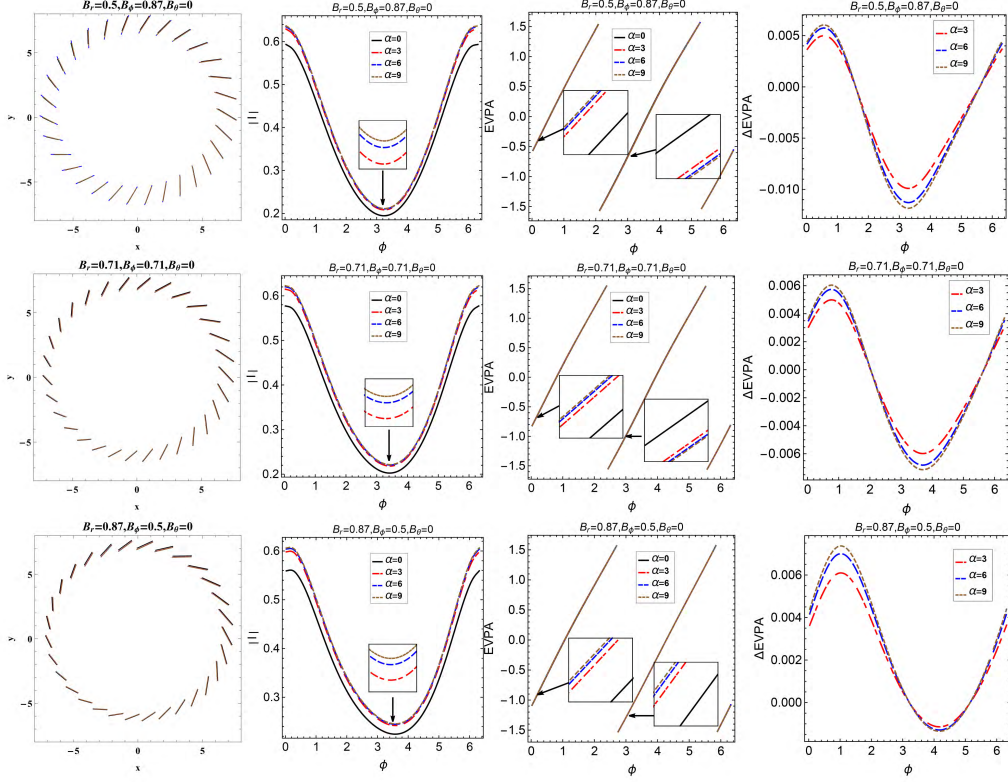


FIG. 3: Effects of the MOG parameter α on the polarized vector and EVPA in the Kerr-MOG black hole spacetime (3) for the equatorial magnetic field. Here $r_s = 6$, $a = -0.3$, $\theta_o = 20^\circ$, $\beta_\nu = 0.3$, and $\chi = -90^\circ$.

different observer inclination angle θ_o are shown in Fig.(5). It is shown that with the increase of the observer inclination angle θ_o , the region where polarization intensity and EVPA increase with α becomes narrow.

Figs.(6)-(8) also present the dependence of the polarization intensity and the EVPA on the MOG parameter α in the case where the magnetic field is perpendicular to the equatorial plane. Results show that the effects of MOG parameter α on the polarized vector and EVPA also depend on the azimuthal coordinate ϕ of the point in the emitting ring, the black hole spin parameter, the fluid direction angle and the observer inclination angle. The dependence of polarization intensity and EVPA with the MOG parameter α vary periodically with the azimuthal coordinate ϕ . For the fixed $\theta_o = 20^\circ$ and $\chi = -90^\circ$, as ϕ varies in the range $(0, 2\pi)$, the polarization intensity and EVPA firstly decrease with α , then increase and finally decrease once again. Similarly, for the different spin parameter a , the dependence of polarization intensity and EVPA on α is also qualitatively similar in this case. With the increase of χ , the region of the polarization intensity increasing with α increases, but the region for the EVPA increasing with α decreases. As the observer inclination angle θ_o increases, the polarization intensity gradually becomes a monotonically increasing function of α , but the change tendency of EVPA with α is similar to that in the case of the low inclination angle θ_o . Moreover, the

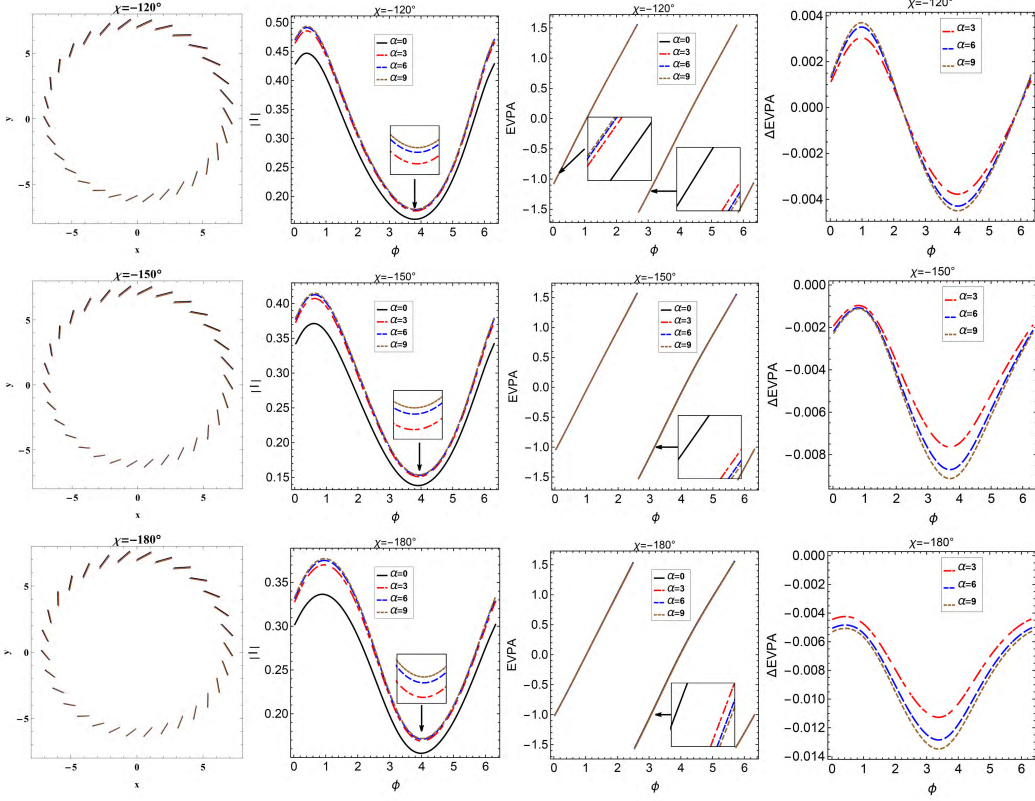


FIG. 4: Effects of the MOG parameter α on the polarized vector and EVPA in the Kerr-MOG black hole spacetime (3) for the different fluid direction angle χ . Here $r_s = 6$, $a = -0.3$, $\theta_o = 20^\circ$, $\beta_\nu = 0.3$, $B_r = 0.87$, $B_\phi = 0.5$ and $B_\theta = 0$.

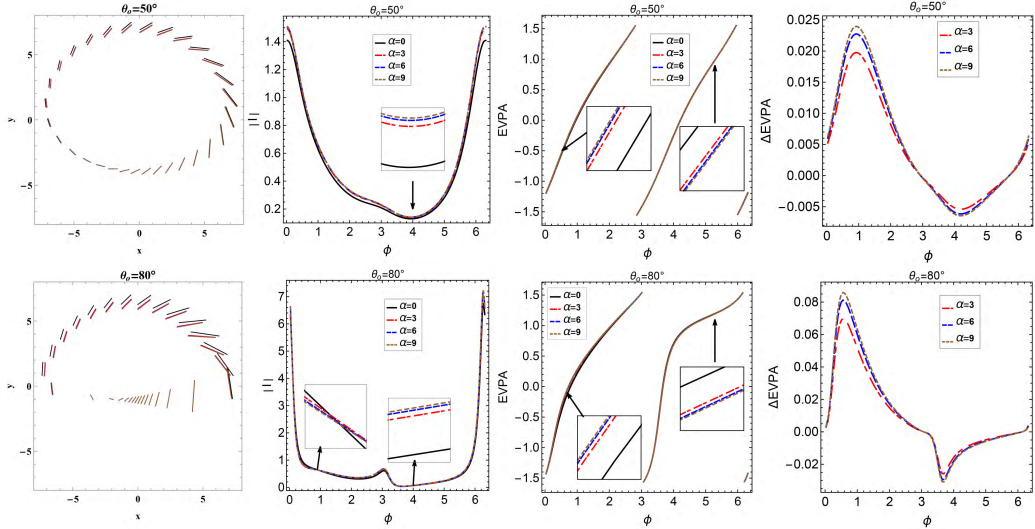


FIG. 5: Effects of the MOG parameter α on the polarized vector and EVPA in the Kerr-MOG black hole spacetime (3) for the different observer inclination angle θ_o . Here $r_s = 6$, $a = -0.3$, $\beta_\nu = 0.3$, $\chi = -90^\circ$, $B_r = 0.87$, $B_\phi = 0.5$ and $B_\theta = 0$.

region where EVPA increases with α becomes narrow in the high inclination angle case.

Figs.(9)-(11) show the effects of the MOG parameter α on Stokes $Q - U$ loop patterns in the image of the

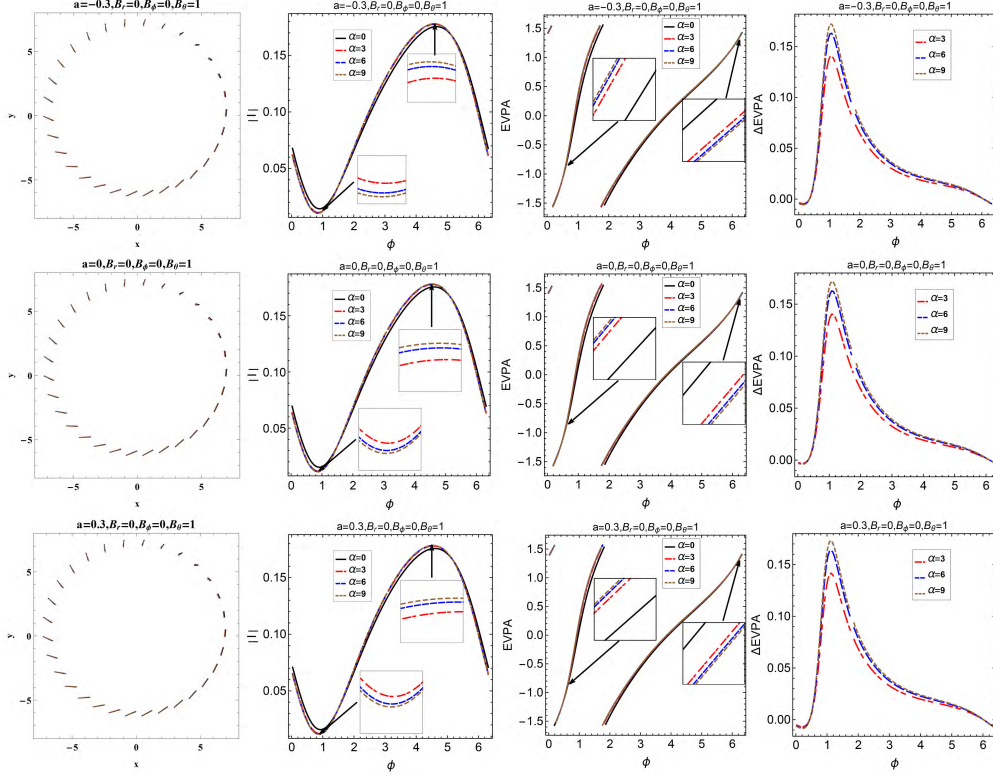


FIG. 6: Effects of the MOG parameter α on the polarized vector and EVPA in the Kerr-MOG black hole spacetime (3) for different a in the case with the magnetic field owned only the vertical component B_θ . Here $r_s = 6$, $\theta_o = 20^\circ$, $\chi = -90^\circ$, $\beta_\nu = 0.3$, and $B_\theta = 1$.

emitting ring. In general, there are two loops enclosing the origin in the $Q - U$ plane. Effects of the MOG parameter α on the $Q - U$ diagram depend heavily on the magnetic field configuration, the fluid velocity, the observation inclination angle and the spin parameter of black hole. As the magnetic field lies in the equatorial plane, the observed two Stokes $Q - U$ loops increase with the MOG parameter α for the observer with $\theta_o = 20^\circ$ and different fluid direction angle χ . For the high observation inclination angle, the sizes of two loops increases with α although the inner loop dramatically shrinks. As the magnetic field is vertical to the equatorial plane, the size of the outer loop increases and the inner loop decreases with α for the observer with $\theta_o = 20^\circ$ and different fluid direction angle χ . For the high observation inclination angle, the inner loop vanishes and the change of loop size with the MOG parameter α becomes more complicated. For the fixed α , as the spin parameter increases, Fig.(12) shows that the inner loop increases for different magnetic fields. However, the outer loop decreases with a as the magnetic field lies in the equatorial plane, and its no longer changes monotonously with a in the case of with the vertical magnetic field. Moreover, for the fixed α , the changes of the $Q - U$ loop patterns with the magnetic field configuration, the fluid velocity and the observation inclination angle are similar to those in the Kerr black hole case.

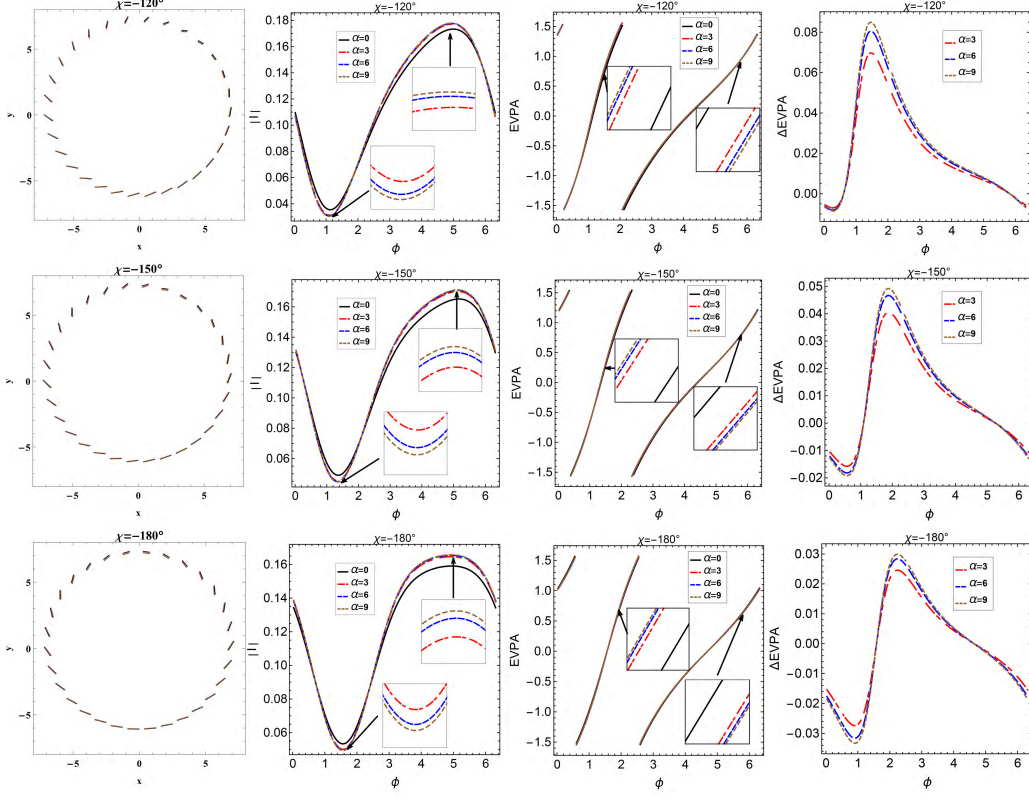


FIG. 7: Effects of the MOG parameter α on the polarized vector and EVPA in the Kerr-MOG black hole spacetime (3) for different χ in the case where magnetic field has only the vertical component B_θ . Here $r_s = 6$, $a = -0.3$, $\theta_o = 20^\circ$, $\beta_\nu = 0.3$, and $B_\theta = 1$.

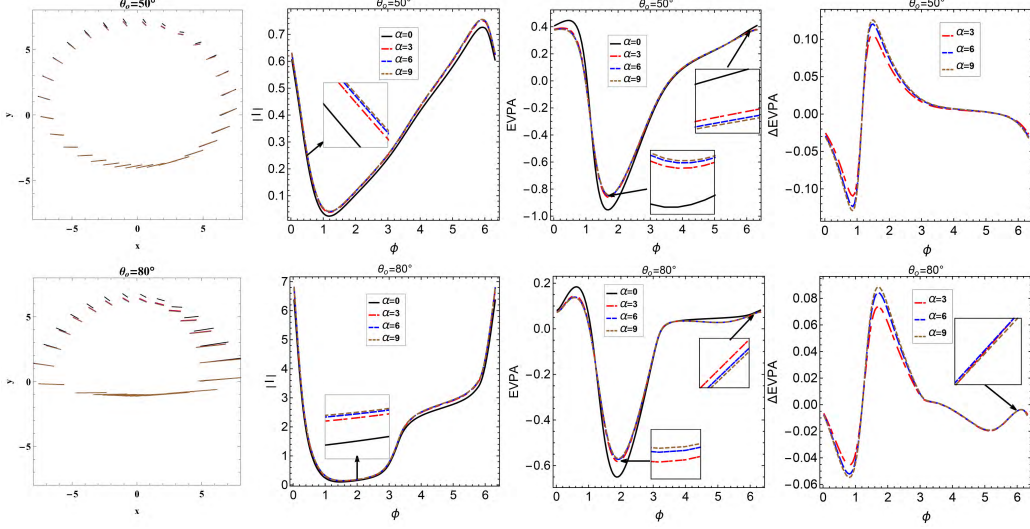


FIG. 8: Effects of the MOG parameter α on the polarized vector and EVPA in the Kerr-MOG black hole spacetime (3) for different θ_o in the case where magnetic field has only the vertical component B_θ . Here $r_s = 6$, $a = -0.3$, $\beta_\nu = 0.3$, $\chi = -90^\circ$, and $B_\theta = 1$.

Finally, Fig.(13) gives a comparison of the polarization image between a Kerr-MOG black hole and M87* black hole. Results show that the polarimetric images of Kerr-MOG black hole for different α own some spiral

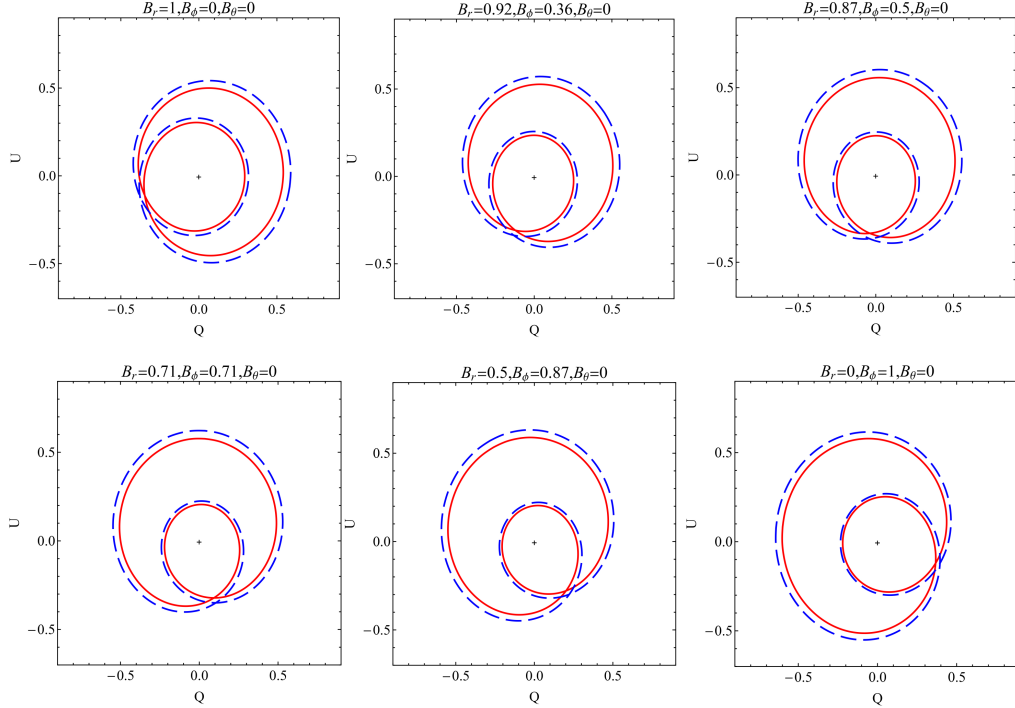


FIG. 9: Effects of the MOG parameter α on the $Q - U$ diagram for different equatorial magnetic fields in the Kerr-MOG black hole (3). Here $r_s = 6$, $\theta_o = 20^\circ$, $a = -0.3$, $\beta_\nu = 0.3$, and $\chi = -90^\circ$. The blue dashed line and the red solid line correspond to the cases with the MOG parameter $\alpha = 9$ and $\alpha = 0$, respectively. Black crosshairs indicate the origin of each plot.

structures and their polarization patterns are similar to those of M87* observed in [8, 9]. The small difference in the polarization images in Fig.(13) implies that there remains some possibility for the STVG-MOG theory.

IV. SUMMARY

This study investigated the polarized images of the emitting ring around a Kerr-MOG black hole with an additional dimensionless parameter α . The results show that for the fixed MOG parameter α , the change of the polarization vector in the image plane with the spin parameter, the magnetic field configuration, the fluid velocity and the observation inclination angle are similar to those in the Kerr black hole case. The effects of the MOG parameter α on the observed polarization vector depend on the black hole parameters, the material distribution around black hole and the observation inclination angle. For the cases where the magnetic field lies in the equatorial plane, the polarization intensity increase with the MOG parameter α in the lower observation inclination angle case, and no longer varies monotonously in the higher observation inclination angle case. The change of EVPA with α becomes more complicated and it also depends on the ratio between the radial component and the azimuthal component of magnetic field B_r/B_ϕ . As the magnetic field

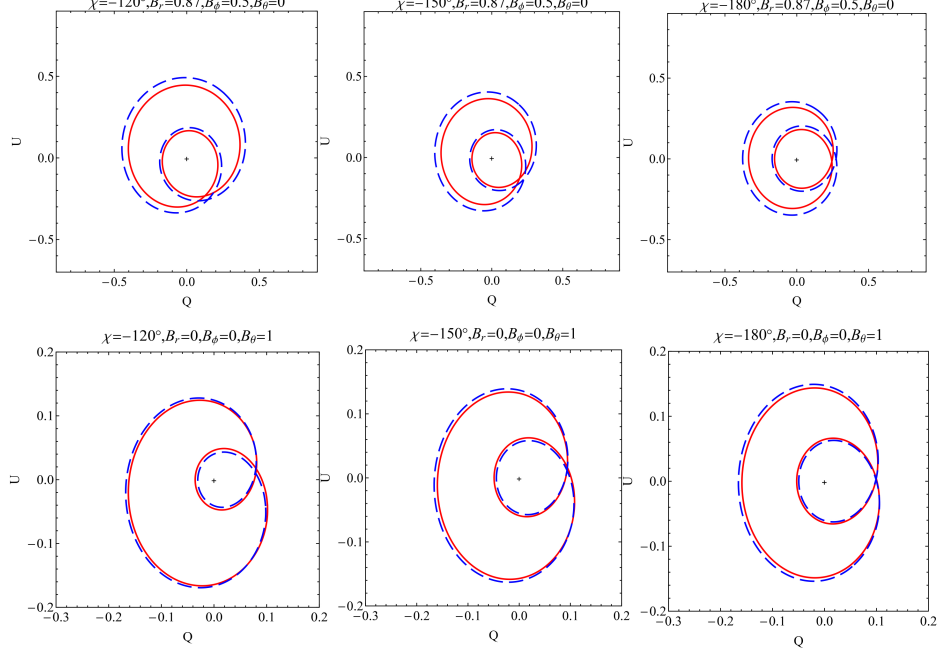


FIG. 10: Effects of the MOG parameter α on the $Q - U$ diagram for different fluid velocity angle χ in the Kerr-MOG black hole (3). Here $r_s = 6$, $\theta_o = 20^\circ$, $a = -0.3$, and $\beta_\nu = 0.3$. The top and bottom rows correspond to the equatorial magnetic field and the vertical one, respectively. The blue dashed line and the red solid line correspond to the cases with the MOG parameter $\alpha = 9$ and $\alpha = 0$, respectively. Black crosshairs indicate the origin of each plot.

is perpendicular to the equatorial plane, the dependence of polarization intensity and EVPA with the MOG parameter α vary periodically with the azimuthal coordinate ϕ in the lower observation inclination angle case. As the observer inclination angle θ_o increases, the polarization intensity gradually becomes a monotonically increasing function of α , but the change tendency of EVPA with α is similar to that in the case of the low inclination angle θ_o and the region where EVPA increases with α becomes more narrow.

Effects of the MOG parameter α on the $Q - U$ diagram also depend heavily on the magnetic field configuration, the fluid velocity, the observation inclination angle and the spin parameter of black hole. In the case with the lower observed inclination, the size of the $Q - U$ loop increases with α as the magnetic field lies in the equatorial plane, and the size of the outer loop increases and the inner loop decreases as the magnetic field is vertical to the equatorial plane. In the higher inclination angle case, the sizes of two loops increase with α although the inner loop dramatically shrinks as the magnetic field lies in the equatorial plane, however, as the magnetic field is vertical to the equatorial plane, the inner loop vanishes and the change of loop size with the MOG parameter α becomes more complicated. Moreover, for the fixed α , as the spin parameter increases, the inner loop increases for different magnetic fields. However, the outer loop decreases with a as the magnetic field lies in the equatorial plane, and its no longer changes monotonously with a in the case of with the vertical

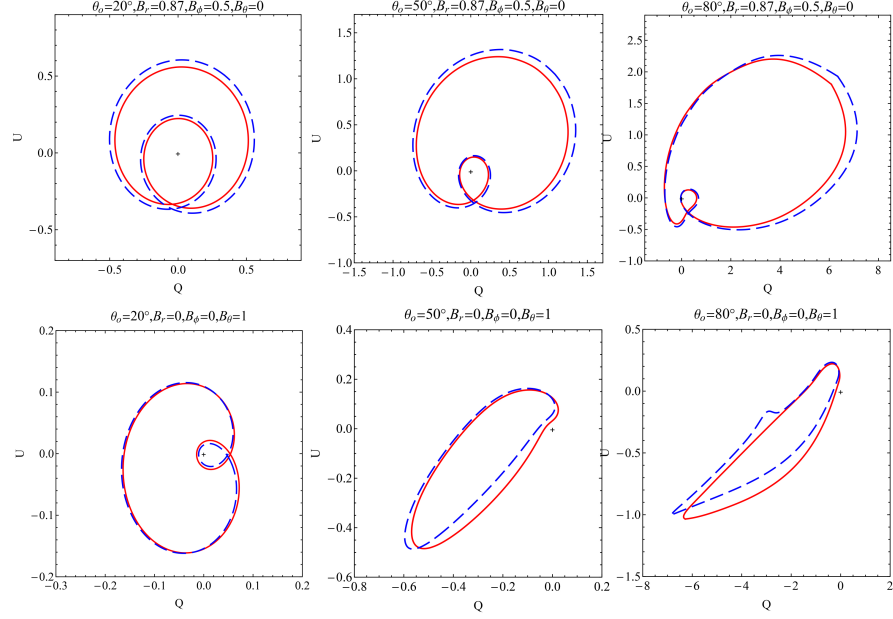


FIG. 11: Effects of the MOG parameter α on the $Q - U$ diagram for different observation inclination angle θ_o in the Kerr-MOG black hole (3). Here $r_s = 6$, $a = -0.3$, $\beta_\nu = 0.3$ and $\chi = -90^\circ$. The top and bottom rows represent the equatorial and vertical magnetic field, respectively. The blue dashed line and the red solid line correspond to the cases with the MOG parameter $\alpha = 9$ and $\alpha = 0$, respectively. Black crosshairs indicate the origin of each plot.

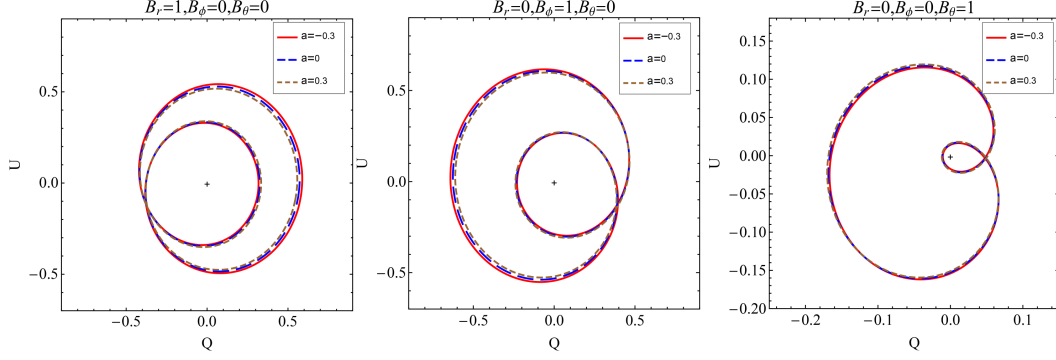


FIG. 12: Effects of the spin parameter a on the $Q - U$ diagram for different magnetic fields in the Kerr-MOG black hole (3). Here $r_s = 6$, $\theta_o = 20^\circ$, $\alpha = 9$, $\beta_\nu = 0.3$ and $\chi = -90^\circ$. Black crosshairs indicate the origin of each plot.

magnetic field. Finally, making a comparison of the polarization images between Kerr-MOG black hole and M87*, there are some similar spiral structures appeared in the polarimetric images of two black holes. Our result also implies that there remains some possibility for the STVG-MOG theory.

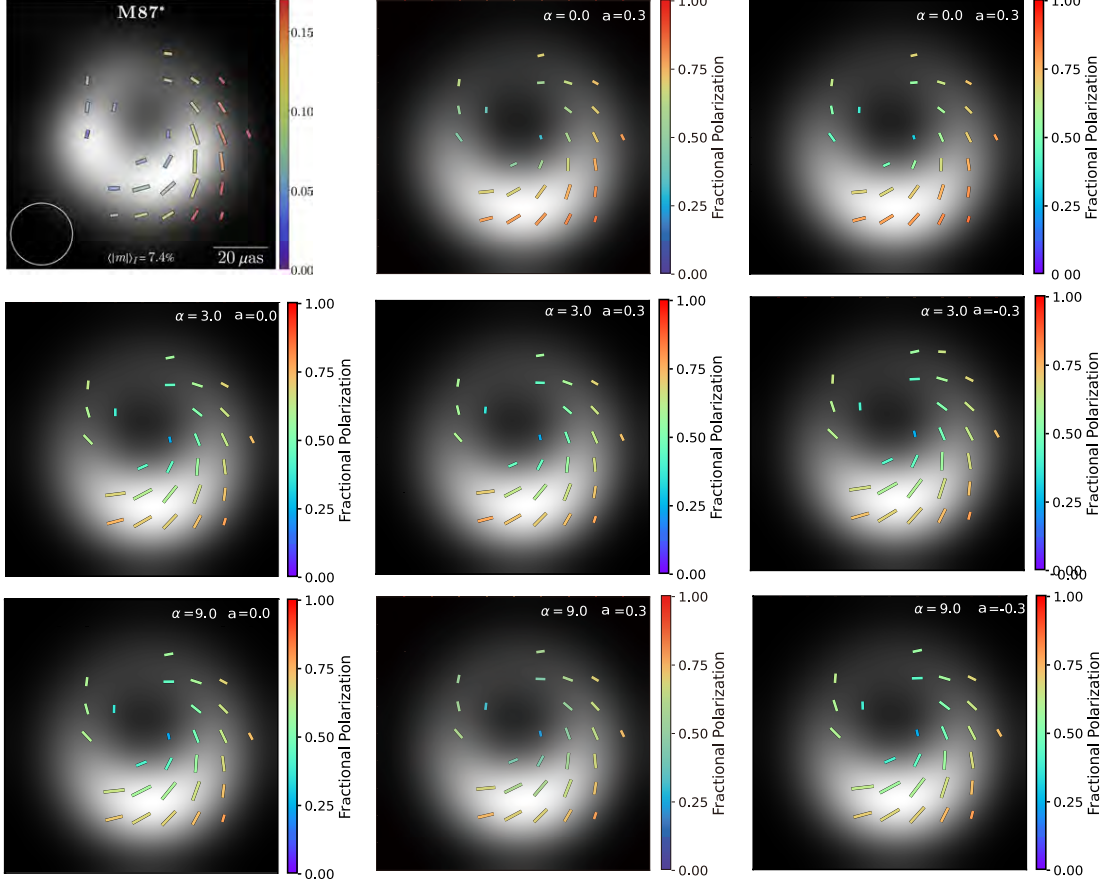


FIG. 13: Comparison between the polarimetric image of Kerr-MOG black hole and the black hole M 87* [8, 9]. Here $\theta = 17^\circ$, $\beta_\nu = 0.4$, $\chi = -150^\circ$, $B_r = 0.87$, $B_\phi = 0.5$ and $B_\theta = 0$.

V. ACKNOWLEDGMENTS

This work was supported by the National Natural Science Foundation of China under Grant No.11875026, 11875025 and 12035005.

-
- [1] The Event Horizon Telescope Collaboration, *First M87 Event Horizon Telescope Results. I. The Shadow of the Supermassive Black Hole*, *Astrophys. J. Lett.* **875**, L1 (2019).
 - [2] The Event Horizon Telescope Collaboration, *First M87 Event Horizon Telescope Results. II. Array and Instrumentation*, *Astrophys. J. Lett.* **875**, L2 (2019).
 - [3] The Event Horizon Telescope Collaboration, *First M87 Event Horizon Telescope Results. III. Data Processing and Calibration*, *Astrophys. J. Lett.* **875**, L3 (2019).
 - [4] The Event Horizon Telescope Collaboration, *First M87 Event Horizon Telescope Results. IV. Imaging the Central Supermassive Black Hole*, *Astrophys. J. Lett.* **875**, L4 (2019).
 - [5] The Event Horizon Telescope Collaboration, *First M87 Event Horizon Telescope Results. V. Physical origin of the asymmetric ring*, *Astrophys. J. Lett.* **875**, L5 (2019).
 - [6] The Event Horizon Telescope Collaboration, *First M87 Event Horizon Telescope Results. VI. The Shadow and*

- Mass of the Central Black Hole*, *Astrophys. J. Lett.* **875**, L6 (2019).
- [7] The Event Horizon Telescope Collaboration, *First Sagittarius A* Event Horizon Telescope Results. I. The Shadow of the Supermassive Black Hole in the Center of the Milky Way*, *Astrophys. J. Lett.* **930**, L12 (2022).
- [8] The Event Horizon Telescope Collaboration, *First M87 Event Horizon Telescope Results. VII. Polarization of the Ring*, *Astrophys. J. Lett.* **875**, L7 (2019).
- [9] The Event Horizon Telescope Collaboration, *First M87 Event Horizon Telescope Results. VIII. Magnetic Field Structure near The Event Horizon*, *Astrophys. J. Lett.* **875**, L8 (2019).
- [10] R. Narayan, D. C. M. Palumbo, M. D. Johnson, Z. Gelles, E. Himwich, D. O. Chang, A. Ricarte, J. Dexter, C. F. Gammie, A. A. Chael, and The Event Horizon Telescope Collaboration, *The Polarized Image of a Synchrotron-emitting Ring of Gas Orbiting a Black Hole*, *Astrophys. J.* **912**, 35 (2021).
- [11] Z. Gelles, E. Himwich, D. C. M. Palumbo, M. D. Johnson, *Polarized Image of Equatorial Emission in the Kerr Geometry*, *Physical Review D* 104, (2021) 044060. arXiv:2105.09440.
- [12] X. Qin, S. Chen, J. Jing, *Polarized image of an equatorial emitting ring around a 4D Gauss-Bonnet black hole*, arXiv: 2111.10138.
- [13] X. Liu, S. Chen, J. Jing, *Polarization distribution in the image of a synchrotron emitting ring around regular black holes*, arXiv: 2205.00391.
- [14] Z. Zhang, S. Chen, X. Qin and J. Jing, *Polarized image of a Schwarzschild black hole with a thin accretion disk as photon couples to Weyl tensor*, *Eur. Phys. J. C.* **81**, 11 (2021) 991. arXiv: 2106.07981. (2021).
- [15] Z. Zhang, S. Chen, and J. Jing, *Image of Bonnor black dihole with a thin accretion disk and its polarization information*, arXiv: 2205.13396 (2021).
- [16] H. Zhu and M. Guo, *Polarized image of synchrotron radiations of hotspots in Schwarzschild-Melvin black hole spacetime*, arXiv: 2205.04777.
- [17] Z. Hu, Y. Hou, H. Yan, M. Guo, and B. Chen, *Electromagnetic radiations and polarized images of synchrotron radiations in curved spacetime*, arXiv: 2203.02908.
- [18] P. A. Connors, T. Piran, and R. F. Stark, *Polarization features of X-ray radiation emitted near black holes*, *Astrophys. J.* **235**, 224-244 (1980).
- [19] B. C. Bromley, F. Melia, and S. Liu, *Polarimetric Imaging of the Massive Black Hole at the Galactic Center*, *Astrophys. J. Lett.* **555**, L83-L86 (2001).
- [20] L.X. Li, R. Narayan, and J. E. McClintock, *Inferring the Inclination of a Black Hole Accretion Disk from Observations of its Polarized Continuum Radiation*, *Astrophys. J.* **555** no. 1, 847-865 (2009).
- [21] R. V. Shcherbakov, R. F. Penna, and J. C. McKinney, *Sagittarius A* Accretion Flow and Black Hole Parameters from General Relativistic Dynamical and Polarized Radiative Modeling*, *Astrophys. J.* **755**, 847-865 (2012).
- [22] J. Dexter, *A public code for general relativistic, polarised radiative transfer around spinning black holes*, *MNRAS.* **462** no. 1, 115-136 (2016).
- [23] R. Gold, J. C. McKinney, M. D. Johnson, and S. S. Doeleman, *Probing the Magnetic Field Structure in Sgr A* on Black Hole Horizon Scales with Polarized Radiative Transfer Simulations*, *Astrophys. J.* **837**, 180 (2017).
- [24] F. Marin, M. Dovčiak, F. Muleri, F. F. Kislak, and H. S. Krawczynski, *Predicting the X-ray polarization of type 2 Seyfert galaxies*, *MNRAS.* **473**, 1286-1316 (2016).
- [25] A. Jim'enez-Rosales and J. Dexter, *The impact of Faraday effects on polarized black hole images of Sagittarius A**, *MNRAS.* **478**, 1875-1883 (2018).
- [26] D. C. M. Palumbo, G. N. Wong, and B. S. Prather, *Discriminating accretion states via rotational symmetry in simulated polarimetric images of m87*, *Astrophys. J.* **894**, 156 (2020).
- [27] M. Moscibrodzka, *General relativistic polarized radiative transfer with inverse-Compton scatterings*, *MNRAS.* **491** no. 4, 4807-4815 (2020).
- [28] M. Moscibrodzka, A. Janiuk, and M. De Laurentis, *Unraveling circular polarimetric images of magnetically arrested accretion flows near event horizon of a black hole*, arXiv: 2103.00267. (2021)
- [29] V. C. Rubin, E. M. Burbidge, G. R. Burbidge, K. H. Prendergast, *The Rotation and Mass of the Inner Parts of NGC 4826*, *Astrophys. J.* **141**, 885 (1965).

- [30] V. C. Rubin, W. K. Ford, *Rotation of the Andromeda Nebula from a Spectroscopic Survey of Emission Regions*, *Astrophys. J.* **159**, 379 (1970).
- [31] J. W. Moffat, *Scalar-Tensor-Vector Gravity Theory*, *J. Cosmol. Astropart. Phys.* **2006**(3), 004 (2006).
- [32] J. W. Moffat, S. Rahvar, *The MOG weak field approximation and observational test of galaxy rotation curves*, *Mon. Not. Roy. Astron. Soc.* **436**, 1439 (2013).
- [33] J. W. Moffat and V. T. Toth, *Rotational Velocity Curves in the Milky Way as a Test of Modified Gravity*, *Phys. Rev. D* **91**, 043004 (2015), arXiv:1411.6701 [astro-ph.GA].
- [34] J. W. Moffat, *Gravitational Lensing in Modified Gravity and the Lensing of Merging Clusters without Dark Matter*, astro-ph/0608675.
- [35] J. R. Brownstein, J. W. Moffat, *The Bullet Cluster 1E0657-558 evidence shows Modified Gravity in the absence of Dark Matter*, *Mon. Not. Roy. Astron. Soc.* **382**, 29 (2007).
- [36] J. W. Moffat, S. Rahvar, *The MOG Weak Field approximation II. Observational test of Chandra X-ray Clusters*, *Mon. Not. Roy. Astron. Soc.* **441**, 3724 (2014).
- [37] J. W. Moffat, *LIGO GW150914 and GW151226 Gravitational Wave Detection and Generalized Gravitation Theory (MOG)*, *Phys. Lett. B* **763**, 427 (2016).
- [38] M. A. Green, J. W. Moffat, V. T. Toth, *Modified Gravity (MOG), the speed of gravitational radiation and the event GW170817/GRB170817A*, *Phys. Lett. B* **780**, 300 (2018).
- [39] J. W. Moffat, *Black holes in modified gravity (MOG)*, *Eur. Phys. J. C* **75**, 175 (2015). arXiv:1412.5424.
- [40] L. Manfredi, J. Mureika, and J. W. Moffat, *Quasinormal modes of modified gravity (MOG) black holes*, *Phys. Lett. B* **779**, 492 (2018). arXiv:1711.03199.
- [41] J. W. Moffat, *Modified gravity black holes and their observable shadows*, *Eur. Phys. J. C* **75**, 130 (2015). arXiv:1502.01677.
- [42] H. Wang, Y. Xu and S. Wei, *Shadows of Kerr-like black holes in a modified gravity theory*, *J. Cosmol. Astropart. Phys.* **1903**, 046 (2019). arXiv:1810.12767.
- [43] J. R. Mureika, J. W. Moffat, and M. Faizal, *Black hole thermodynamics in modified gravity (MOG)*, *Phys. Lett. B* **757**, 528 (2016). arXiv:1504.08226.
- [44] H. C. Lee and Y. J. Han, *Inner-most stable circular orbit in Kerr-MOG black hole*, *Eur. Phys. J. C* **77**, 655 (2017). arXiv:1704.02740.
- [45] M. Sharif and M. Shahzadi, *Particle dynamics near Kerr-MOG black hole*, *Eur. Phys. J. C* **77**, 363 (2017). arXiv:1705.03058.
- [46] S. Hussain and M. Jamil, *Timelike geodesics of a modified gravity black hole immersed in an axially symmetric magnetic field*, *Phys. Rev. D* **92**, 043008 (2015). arXiv:1508.02123.
- [47] D. Perez, F. G. L. Armengol, and G. E. Romero, *Accretion disks around black holes in Scalar-Tensor-Vector gravity*, *Phys. Rev. D* **95**, 104047 (2017). arXiv:1705.02713.
- [48] P. Sheoran, A. Herrera-Aguilar, and U. Nucamendi, *Mass and spin of a Kerr black hole in modified gravity and a test of the Kerr black hole hypothesis*, *Phys. Rev. D* **97**, 124049 (2018). arXiv:1712.03344.
- [49] J. W. Moffat, *Misaligned spin merging black holes in modified gravity (MOG)*, arXiv:1706.05035.
- [50] S. Wei, Y. Liu, *Merger estimates for rotating Kerr black holes in modified gravity*, *Phys. Rev. D* **98**, 024042 (2018). arXiv:1803.09530.
- [51] S. E. Gralla and A. Lupsasca, *Lensing by Kerr black holes*, *Physical Review D* **101**, 044031 (2020). arXiv:1910.12873.
- [52] M. Walker and R. Penrose, *On quadratic first integrals of the geodesic equations for type {2,2} spacetimes*, *Commun. Math. Phys.* **18**, 265 (2001).
- [53] S. Chandrasekhar, *The mathematical theory of black holes*. 1985
- [54] E. Himwich, M. D. Johnson, A. Lupsasca, and A. Strominger, *Universal polarimetric signatures of the black hole photon ring*, *Phys. Rev. D.* **101**, 084020 (2020).